NANO LETTERS

Letter

pubs.acs.org/NanoLett

# Generating and Separating Twisted Light by gradient−rotation Split-Ring Antenna Metasurfaces

Jinwei Zeng, Ling Li, Xiaodong Yang,* and Jie Gao*

Department of Mechanical and Aerospace Engineering, Missouri University of Science and Technology, Rolla, Missouri 65409, United States

**ABSTRACT:** Nanoscale compact optical vortex generators promise substantially significant prospects in modern optics and photonics, leading to many advances in sensing, imaging, quantum communication, and optical manipulation. However, conventional vortex generators often suffer from bulky size, low vortex mode purity in the converted beam, or limited operation bandwidth. Here, we design and demonstrate gradient−rotation split-ring antenna metasurfaces as unique spin-to-orbital angular momentum beam converters to simultaneously generate and separate pure optical vortices in a broad wavelength range. Our proposed design has the potential for realizing miniaturized on-chip OAM-multiplexers, as well as enabling new types of metasurface devices for the manipulation of complex structured light beams.

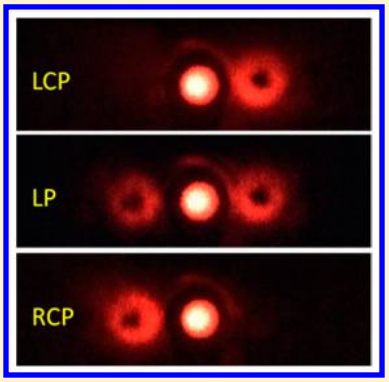


**KEYWORDS:** *Optical vortex, metasurfaces, Pancharatnam-Berry phase optical elements, plasmonic split-ring antenna, orbital angular momentum*

Featured by helical-structured wavefront and orbital angular momentum (OAM), optical vortices have attracted great attention in modern optics and photonics due to their unprecedented promising applications in high-resolution imaging, remote sensing, quantum information processing, and optical manipulation.[1−5] Recently, the generation and manipulation of optical vortices have been remarkably enhanced by utilizing the properly designed metamaterials and metasurfaces.[6−25] The metamaterials and metasurfaces are artificial, subwavelength structured materials capable of realizing unconventional electromagnetic properties not existing in nature, such as abrupt phase or polarization change, negative index of refraction, near-zero permittivity or permeability, extraordinary anisotropy, and so forth.[26−30] Metamaterials and metasurfaces have the capabilities of tailoring the intensity, phase, and polarization of light beams at subwavelength scale, enabling the development of ultracompact vortex generators and structured beam converters and making it one step closer to realizing the OAM-based photonic integrated circuits.[6,7,15,23]

One major challenge of the current vortex generators is how to create optical vortices with high mode purity in a broad wavelength range. The broadband operation is especially desirable in the applications of free-space or fiber optical communication where OAM and wavelength multiplexing can be simultaneously employed to increase the data density. However, the bandwidth of conventional vortex generators such as spiral phase plates and spatial light modulators is greatly limited by the material dispersion, where the phase modulation based on optical path difference varies as a function of frequency.[31,32] Instead of utilizing direct optical path-based phase shift, one approach to overcome the bandwidth limitation is to consider the space-domain Pancharatnam-Berry phase.[33,34] The Pancharatnam-Berry phase describes the relationship between phase change and polarization conversion when the light beam transmits through an anisotropic optical element, which was first discovered in several pioneering works.[13,18−20,35,36] In the Pancharatnam-Berry phase optical elements (PBOEs), the phase change originates from the geometrical phase that accompanies polarization conversion rather than the optical path differences in conventional diffractive and refractive elements. Optical vortices with arbitrary charges of OAM in broadband operation have been generated by several types of metamaterial or metasurface based PBOEs, including nanorod antennas, nanogratings, V-shape antennas, and other well-designed nanostructures.[6,9,13,16,17,19,21,22] However, the generated vortex beams are usually impure and in mixed states including unconverted or other undesirable beam components. Moreover, the polarization conversion efficiency in the metamaterial or metasurface based PBOEs is often low outside the optimized operation bandwidth.

In order to directly obtain the pure vortex beam component generated by PBOEs in broadband operation, here we propose and demonstrate the gradient−rotation split-ring antenna metasurfaces as unique vortex beam converters, which can produce a complex phase profile containing the superposition of both linear gradient phase and rotation spiral phase, so that the converted vortex beam with high mode purity will be

**Received:** January 27, 2016
**Revised:** April 8, 2016
**Published:** April 19, 2016





DOI: 10.1021/acs.nanolett.6b00360
*Nano Lett.* 2016, 16, 3101−3108

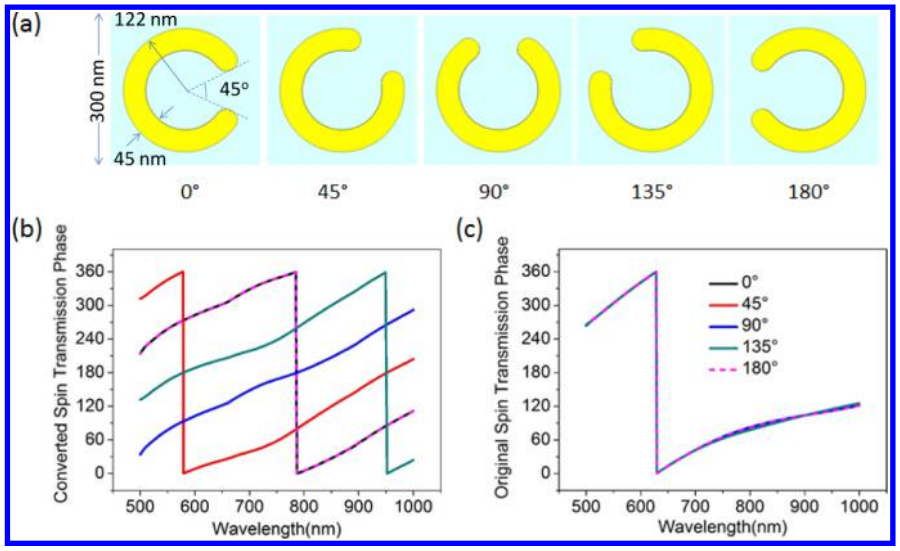


**Figure 1.** (a) The unit cell design of the split-ring antenna at various rotation angles of 0, 45°, 90°, 135°, and 180°, respectively. (b,c) The transmission phase shift spectra of the unit cell for the converted spin component and the original spin component, respectively.

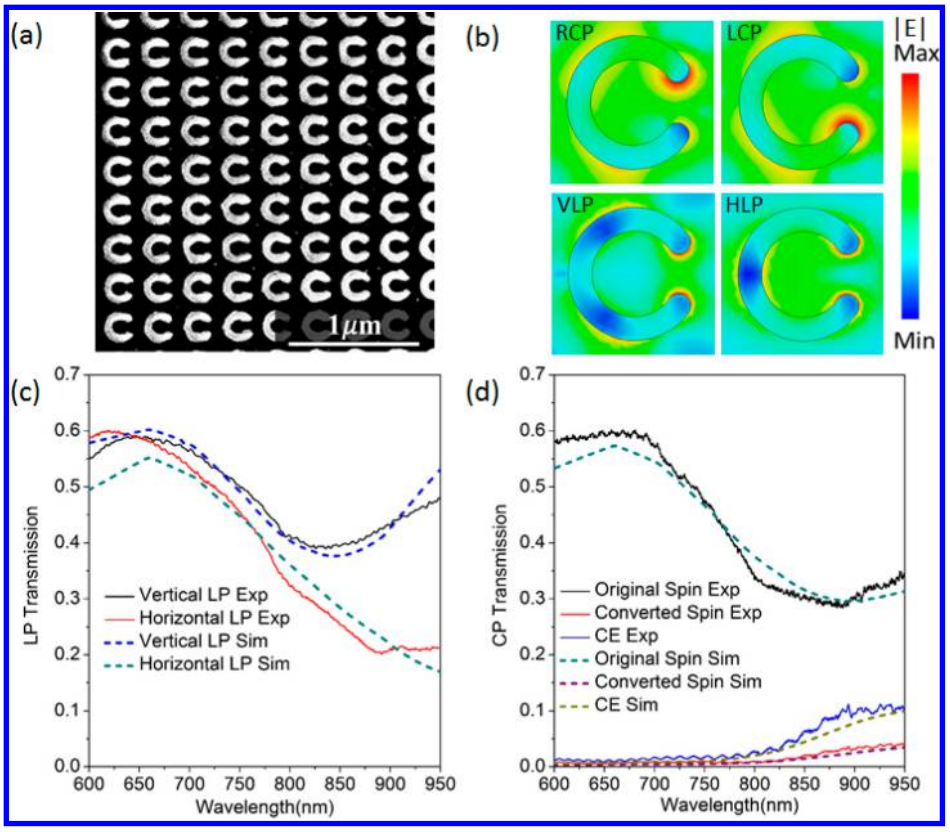


**Figure 2.** (a) One SEM image of the fabricated split-ring antenna homogeneous array. (b) Simulated optical field |*E*| distributions of split-ring antennas under orthogonal polarizations at 900 nm. (c,d) Measured and simulated transmission spectra under linear polarization basis and circular polarization basis, respectively.

separated from the unconverted and other undesirable beam components in a specifically designed diffraction angle. Furthermore, the demonstrated metasurface beam converters operate in broadband and the OAM of the separated vortex beam is independent of wavelength. Our results of simultaneous generation and separation of optical vortex beams using metasurface PBOEs will open new degrees of freedom for building new types of metasurface devices in complex light beam manipulation.

The general principle of PBOEs has been extensively studied by the previous literatures.[13,18−20] It describes the relationship between phase change and polarization conversion as the incident light beam normally transmits through an anisotropic optical element. When the incident beam has circular polarization, the transmitted beam will contain both the original circular polarization (the original spin) component and the converted opposite circular polarization (the converted spin) component. The transmission phase shift of the original



DOI: 10.1021/acs.nanolett.6b00360
*Nano Lett.* 2016, 16, 3101−3108

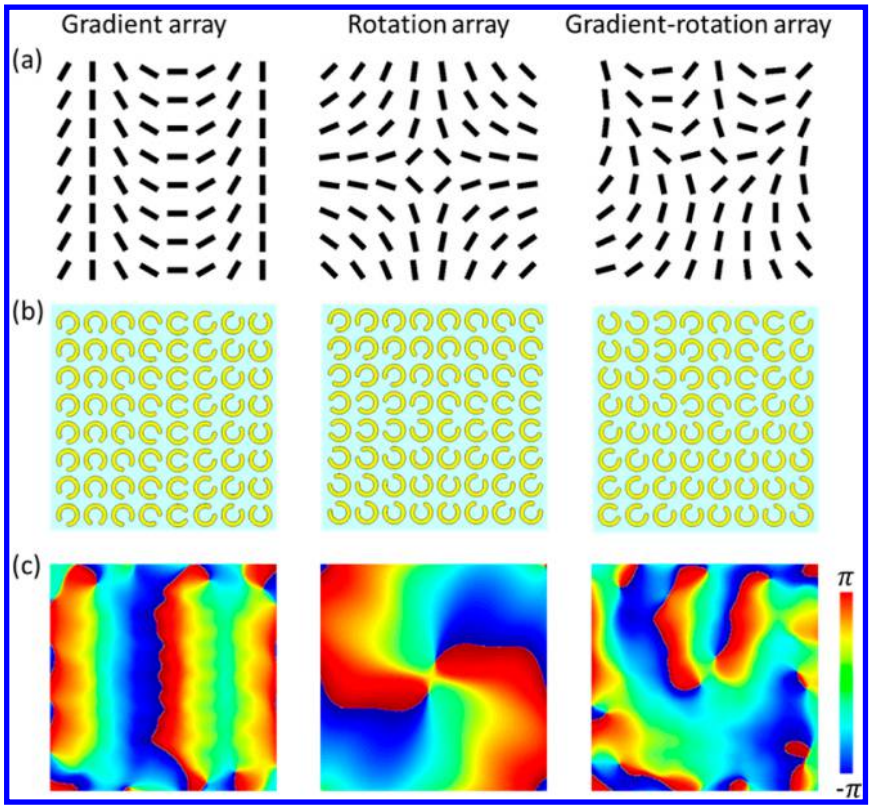


**Figure 3.** (a) Schematics of the optical axis orientation distributions of split-ring antennas for gradient array, rotation array, and gradient−rotation array, respectively. (b) The corresponding split-ring antenna arrays. (c) Simulated near-field phase distributions of the converted spin components from these inhomogeneous antenna arrays.

spin component stays the same against the rotation of anisotropic optical elements, while the absolute transmission phase shift of the converted spin component changes twice as the rotation angle of the optical elements. By arranging the anisotropic metamaterial or metasurface PBOEs into a designed spatially inhomogeneous array, an arbitrary phase profile for the converted spin in the transmitted beam can be created for light beam modulation. The design of the unit cell of PBOEs is critical because the unit cell periodicity is usually altered under the rotation in an inhomogeneous array, which will result in the variation of electromagnetic properties for the unit cell. Therefore, PBOEs with strongly cross-coupled unit cells, such as nanogratings, are often grouped into multiple sections with each section containing several unit cells homogeneously in order to maintain the periodicity properties.[18,20,37] Such PBOEs with strong cross-coupling have a limited flexibility for the complex phase shaping due to the low spatial resolution of phase profile. However, when the unit cell elements are designed to have weak cross-coupling, the phase manipulation can be achieved by only rotating the nanostructure within the unit cell.[14,21,38] In this work, plasmonic split-ring antennas[14,39−43] with weak cross-coupling are used as the unit cell elements of PBOEs to construct the metasurface beam converter. The split-ring antennas have the advantages of broadband operation and high polarization anisotropy, together with rotation flexibility. As shown in Figure 1a, the split-ring antenna is convenient to rotate within the unit cell due to its unique C-shape geometry, providing the flexible freedom for the construction of arbitrary anisotropic and inhomogeneous metasurfaces. The split-ring antennas in a thin gold film on glass substrates are designed with FDTD modeling. The unit cell structure is shown in Figure 1a, where the period of the unit cell is 300 nm, the line width of the antenna is 45 nm, the outer radius of the split-ring is 122 nm, and the thickness of the gold film is 50 nm. The antenna has the split angle of 45° with the rounded end. The permittivity of gold is acquired from spectroscopic ellipsometry based on the fitting from a general oscillator model. Figure 1b,c shows the plots of the simulated transmission phase shifts for both the left-handed circular polarization (LCP, the converted spin) component and the input right-handed circular polarization (RCP, the original spin) component of the transmitted output beam from the split-ring antennas in different rotation angles of split-ring antennas without rotating their periodicity. It is shown that in a broadband wavelength range from 500 to 1000 nm, the phase shift variations for the split-ring antennas with different orientations are twice as the rotation angles for the converted spin component, whereas the phase shifts are unchanged at all rotation angles for the original spin component.

The homogeneous periodic array of the designed split-ring antennas is first fabricated and characterized. The pattern is milled by a focus ion beam (FIB) system in a 50 nm thick gold film deposited on glass substrates. The fabricated metasurface area is around 30 $\mu$m by 30 $\mu$m in square and one SEM image of the homogeneous array sample is shown in Figure 2a. Transmission spectra from the sample are then simulated and measured under both linear polarization basis (vertical and horizontal linear polarizations, VLP and HLP) and circular polarization basis. Figure 2b shows the simulated optical field $|E|$ distributions of split-ring antennas under orthogonal polarizations at the wavelength of 900 nm, where strong polarization anisotropy is clearly presented. As shown in Figure



DOI: 10.1021/acs.nanolett.6b00360
*Nano Lett.* 2016, 16, 3101−3108

2c, the measured transmission spectra under linear polarization basis indicate a strong anisotropy for the split-ring antennas in a broadband range especially above the wavelength of 750 nm. The maximum anisotropy is located around 900 nm where the plasmonic resonance occurs. For the transmission under circular polarization basis, the incident beam has a right-handed circular polarization. Figure 2d displays the measured transmission spectra of the original spin component and the converted spin component normalized by the total input optical intensity. The polarization conversion efficiency defined as the intensity ratio between the converted spin component and the total transmitted beam is also plotted. It is shown that the amount of the converted spin increases as the polarization anisotropy gets stronger. The maximum conversion efficiency is around 10% near the wavelength of 900 nm. The simulated transmission spectra under all different polarizations match well with the measured results, proving that the designed split-ring antennas work well as the unit cell elements of PBOEs. By rotating the split-ring antenna orientation within the unit cell, the transmission phase shift of the converted spin component can be modulated in a broad bandwidth.

Next, the inhomogeneous gradient−rotation arrays of split-ring antennas are designed as unique OAM beam converters to simultaneously generate and separate optical vortices with high mode purity in a broad wavelength range. The gradient−rotation array is a superposition of both the gradient array and the rotation array. Figure 3a illustrates the optical axis orientation distributions of split-ring antennas for gradient array, rotation array, and gradient−rotation array, respectively. And the rotation angle $\theta$ of split-ring antenna in gradient array, rotation array, and gradient−rotation array are determined by the following functions, respectively

$$\theta(x, y)_{\text{gradient}} = x\theta_{\text{step}} \tag{1}$$

$$\theta(x, y)_{\text{rotation}} = a\tan2(x - 0.5(N + 1), y - 0.5(N + 1)) \tag{2}$$

$$\theta(x, y)_{\text{gradient-rotation}} = \theta(x, y)_{\text{gradient}} + \theta(x, y)_{\text{rotation}} \tag{3}$$

where $x, y$ represent the position coordinates of the unit cell in the specific column and row in the array, $\theta_{\text{step}}$ is the constant rotation angle change in the gradient array, and $N$ is the number of unit cell along both $x$ and $y$ directions. The antenna orientation angle in the rotation array represents the azimuthal angle, while the orientation angle in the gradient−rotation array is the superposition of the angles used in both the gradient array and the rotation array. The principles of gradient array[14,18,19,22,37−44] and rotation array[6,9,13,16,17,22−25,45] based on plasmonic antenna PBOEs have been widely studied in the previous works. However, the combined gradient−rotation array has not been proposed yet. In this work, the rotation array with antenna orientation angle of a full 360° in an azimuthal circle will be used to generate vortex beam with OAM charge of +2 or −2 in the converted spin component under either right-handed or left-handed circularly polarized incident beam. The gradient array will introduce a phase gradient of $2\theta_{\text{step}}$ along $x$ direction between two adjacent columns for the converted-spin component, so that the beam separation angle $\varphi$ of the converted spin component can be expressed as

$$\varphi = a\tan\left(\frac{\theta_{\text{step}}\lambda}{\pi p}\right) \tag{4}$$

where $p$ is the period of the unit cell, and $\lambda$ is the wavelength of the incident beam. The combined gradient−rotation array will create a complex phase profile containing both gradient phase and spiral phase in the converted spin component, enabling simultaneous optical vortex beam generation and separation. The separated vortex beam is expected to be in completely converted spin polarization with high vortex mode purity. Figure 3b gives the corresponding split-ring antenna arrays according to Figure 3a. The 3D FDTD simulations are then performed to find the near-field phase distributions of the converted spin components in the transmitted beams from these inhomogeneous antenna arrays, as shown in Figure 3c, where the incident beam has a right-handed circular polarization. The gradient step $\theta_{\text{step}}$ is set as 30°. The phase profiles show a clear linear gradient for the gradient array and a spiral pattern for the rotation array. And the phase profile for the gradient−rotation array exhibits the superposition of both the gradient and spiral patterns. Such unique phase distribution will induce the generation and separation of optical vortex beam at the same time.

The designed gradient array and gradient−rotation array metasurfaces are fabricated and characterized for the demonstration of optical beam separation and vortex beam generation. Two gradient arrays with gradient steps $\theta_{\text{step}}$ of 15° and 30° are tested. The SEM images of these fabricated samples are shown in Figure 4a. According to eq 4, the beam separation angles are expected to be 10° and 19.4° for the 15° and 30° gradient array metasurfaces, respectively. Figure 4b displays the measured beam separation from the gradient array samples. The optical

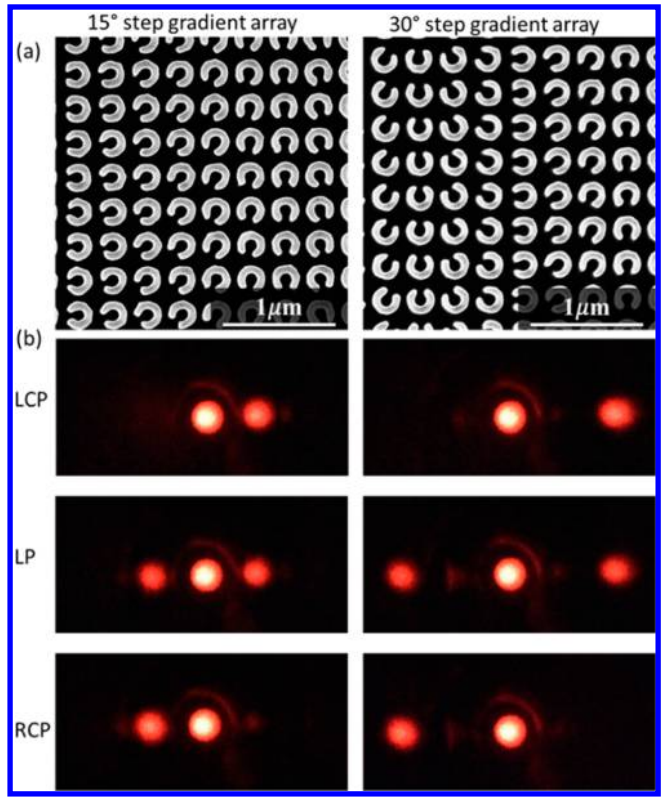


**Figure 4.** (a) SEM images of the gradient arrays with 15° and 30° gradient steps. (b) The captured CCD images of the transmitted diffraction patterns from the gradient array metasurfaces at 633 nm under the incident beams with left-handed circular polarization, linear polarization, and right-handed circular polarization, respectively.



DOI: 10.1021/acs.nanolett.6b00360
*Nano Lett.* 2016, 16, 3101−3108

beam from a HeNe laser at the wavelength of 633 nm is first transmitted through a linear polarizer and a quarter-wave plate to create a circularly polarized beam. Then the beam is focused through the metasurface sample by an objective lens at normal incidence. Finally the transmitted beam is projected on a white screen and the diffraction patterns are captured by a charge-coupled device (CCD) camera. As shown in Figure 4b, the transmitted diffraction patterns from the gradient array samples exhibit unique beam separation properties under specific polarizations. The center bright spot comes from the original spin component of the transmitted beam, which has been selectively attenuated in experiments, while the side dim spots on the left or right are from the beam separation of the converted spin component created by the antenna gradient array. It is observed that the beam separation angle gets increased when the gradient step angle is larger. Furthermore, the direction of beam separation for the converted spin component under the incident beam with left-handed or right-handed circular polarization is just opposite. The beam separation is in both directions for the incident beam with linear polarization, where both left-handed and right-handed circular polarizations are converted. Next, gradient−rotation array metasurfaces with gradient steps $\theta_{step}$ of 15° and 30° are characterized. Figure 5a shows the SEM images of the fabricated samples and Figure 5b displays the measured transmitted diffraction patterns under specific polarizations. Similar to the gradient array samples, the transmitted diffraction patterns from the gradient−rotation array samples show

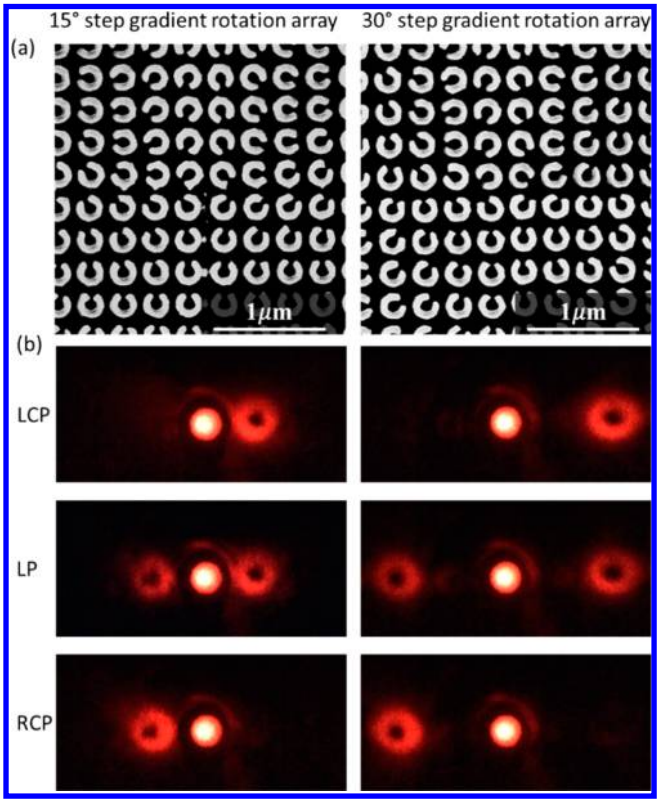


**Figure 5.** (a) SEM images of the gradient−rotation arrays with 15° and 30° gradient steps. (b) The captured CCD images of the transmitted diffraction patterns from the gradient−rotation array metasurfaces at 633 nm under the incident beams with left-handed circular polarization, linear polarization, and right-handed circular polarization, respectively.

polarization-dependent beam separation. In addition, the separated beams present pure donut-shape patterns featuring the generated optical vortices due to the spiral phase profile. It is noteworthy that the gradient−rotation array metasurfaces provide the advantage to generate only one single vortex beam with the designed topological charge in one specified diffraction direction, where the diffraction direction depends on the input circular polarization and the topological charge is determined by the spiral phase profile in metasurface. In contrast, the optical vortex beams generated from the conventional fork gratings[46−49] are always in pairs with opposite topological charges and are located symmetrically in both the positive and negative diffraction orders, where the optical diffraction process is polarization independent and the topological charge depends on the corresponding diffraction order. Therefore, our current metasurface approach gives a robust control for the structured light generation. The separated optical vortices are further characterized by an interferometry setup. The input circularly polarized beam is focused onto the sample at normal incidence. The transmitted beam is observed to include two components, the converted spin component with the generated optical vortex at an oblique diffraction angle and the original spin component maintaining the Gaussian beam wavefront with the beam axis normal to the sample. The original spin component of the transmitted beam is blocked, while the converted spin component is collimated and interfered with the reference beam having the opposite spin to the incident beam. Figure 6 shows the captured intensity profiles of generated optical vortices and the corresponding interferometry patterns from the gradient−rotation array with 30° gradient step, under incident beams with both left-handed and right-handed circular polarizations. The high-quality donut-shape intensity profiles indicate the phase singularities at the center of the generated optical vortices. The interferometry images of the vortex beams exhibit clear double-spiral patterns in opposite orientations under left-handed and right-handed circular polarization incidence, demonstrating an OAM charge of −2 and +2, respectively. These measured vortex beam patterns indicate the high vortex mode purity without including the original Gaussian mode component.

Finally, the broadband response of the gradient−rotation array is characterized with a tunable Ti:sapphire laser for the 15° gradient step sample, covering the wavelength range from 750 to 880 nm. The vortex beam generation and separation across the whole wavelength bandwidth have been observed. As examples, Figure 7 displays the transmitted diffraction patterns captured by an infrared camera under specific polarizations at two wavelengths of 800 and 850 nm. The diffraction patterns show the similar features for vortex generation and separation as those at 633 nm shown in Figure 5, demonstrating the broadband operation capabilities of the metasurface bean converters. In order to determine the vortex beam conversion efficiency, the incident beam power, the separated vortex beam power, and the transmitted straight Gaussian beam power from the gradient−rotation array metasurface are measured across the wavelength range from 750 to 880 nm in a 10 nm step. The vortex beam conversion efficiency is then calculated as the power ratio between the separated vortex beam and the total transmitted beam. Figure 8 plots the measured output beam power and vortex conversion efficiency as functions of the wavelength, which agree well with the corresponding transmission spectra for the homogeneous periodic antenna array as shown in Figure 2d. It is indicated that the vortex beam


DOI: 10.1021/acs.nanolett.6b00360
Nano Lett. 2016, 16, 3101−3108

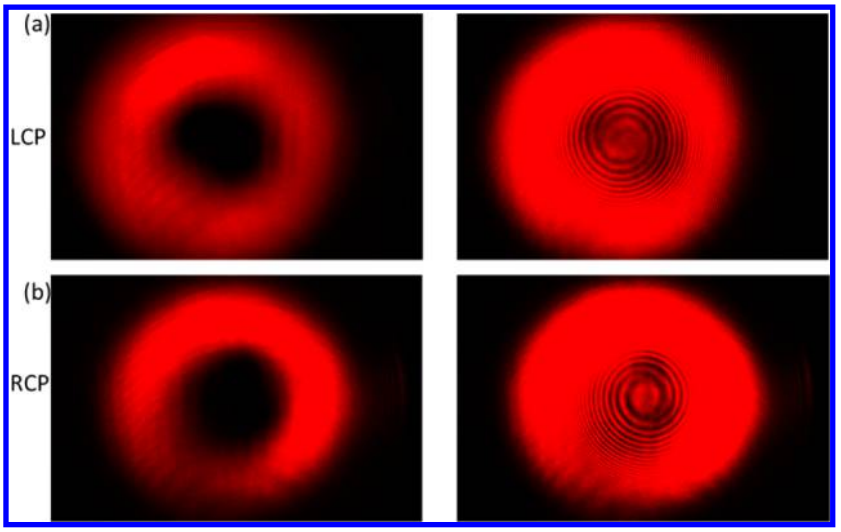


**Figure 6.** Captured intensity profiles of the generated vortices and the corresponding interferometry patterns from the gradient−rotation array with 30° gradient step at 633 nm, under incident beams with (a) left-handed circular polarization and (b) right-handed circular polarization.

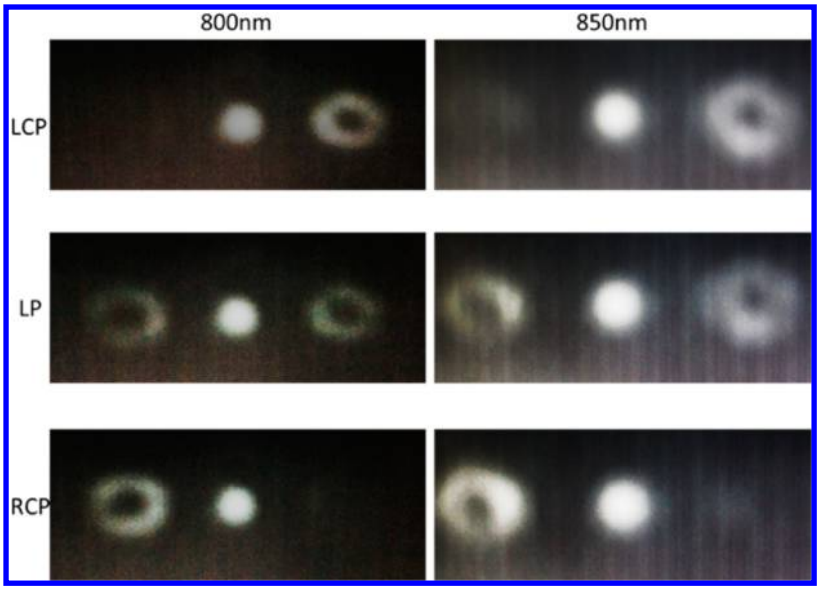


**Figure 7.** Captured infrared images of the transmitted diffraction patterns from the gradient−rotation array sample with 15° gradient step at 800 and 850 nm under the incident beams with left-handed circular polarization, linear polarization, and right-handed circular polarization, respectively.

conversion efficiency for the gradient−rotation array is in close approximation with the polarization conversion efficiency for the homogeneous array, illustrating the reliable PBOE functionality for the designed split-ring antennas. This fact also demonstrates that only the converted spin component with the opposite circular polarization undergoes the designed spiral phase manipulation to produce the vortex beam having high mode purity without including the original Gaussian mode component. As shown in Figure 8, the measured vortex conversion efficiency increases as a function of wavelength and it reaches a value of around 6% at 880 nm.

If the incident Gaussian beam has left-handed circular polarization, the transmitted beam from the gradient−rotation array metasurface contains two components, one is the unconverted original Gaussian mode in the zero diffraction order $\mathbf{E}_o(\mathbf{r}) = \cos(\delta/2)\mathrm{LG}_{0,0}(\mathbf{r})\mathbf{e}_L$ and the other is the converted vortex mode in the designed diffraction direction $\mathbf{E}_v(\mathbf{r}) = e^{i\beta}\sin(\delta/2)\mathrm{LG}_{0,m}(\mathbf{r})\mathbf{e}_R$, where $\delta$ is the birefringent phase retardation of the split-ring antenna unit cell element, $\mathbf{e}_L$ and $\mathbf{e}_R$ stand for left- and right-handed circular polarizations, $\beta$ is the relative phase between the two different polarization states, and $\mathrm{LG}_{p,m}$ represents a Laguerre-Gaussian mode of radial index $p$ and topological charge $m$.[50] It is noted that if the unit cell element behaviors as a half-wave plate where the birefringent phase retardation $\delta$ is equal to $\pi$, there is only the converted vortex beam with the topological charge $m$ in the output without any unconverted Gaussian mode component, leading to the unity conversion efficiency. For other values of the birefringent phase retardation $\delta$, the spin-to-orbital angular momentum conversion is only partial so that a fraction of the input Gaussian beam will remain unchanged in the output and the rest is converted into the vortex beam component, resulting in the conversion efficiency less than one. Our measured low conversion efficiency is because the current birefringent phase retardation in the designed split-ring antenna is much lower than $\pi$. One important reason is that the thickness of gold split-ring antenna is too thin to provide large birefringent phase retardation closed to $\pi$ required for the high conversion


DOI: 10.1021/acs.nanolett.6b00360
*Nano Lett.* 2016, 16, 3101−3108

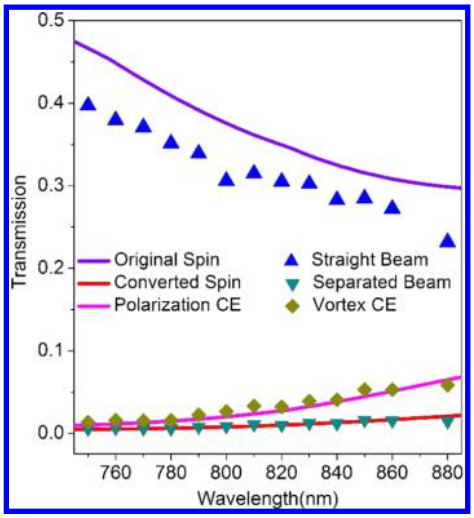


**Figure 8.** Measured separated vortex beam power, the transmitted straight Gaussian beam power, and the vortex conversion efficiency from the gradient−rotation array sample with 15° gradient step (discrete dots). For comparison, the measured transmission spectra from the homogeneous array shown in Figure 2d are also plotted (continuous curves).

efficiency. The general principle to increase the conversion efficiency is to maximize the anisotropy of the antenna structure, by increasing the gold layer thickness and enlarging the split angle of the split-ring antenna. However, the realization of the half-wave plate unit cell element using plasmonic antennas is still quite challenging. As a result, in the previous studies[17] the output vortex modes generated from metasurfaces are not pure due to the unconverted Gaussian mode component. Here, the issues of vortex mode purity and conversion efficiency are separated by utilizing the gradient−rotation array metasurfaces. Now, pure vortex beams are generated and separated from the input Gaussian beams even though the conversion efficiency is extremely low in some wavelength range. The conversion efficiency can be further improved by optimizing the antenna geometries in order to increase the output power of the generated vortex beams.

In summary, we have designed and demonstrated the gradient−rotation split-ring antenna metasurfaces as a new type of vortex beam converters to simultaneously generate and separate optical vortices with high mode purity in a broad wavelength range. The split-ring antenna structure serves as an excellent PBOE capable of producing arbitrary phase shift in the converted spin component by rotating the antenna element in the unit cell. Our demonstrated gradient−rotation array metasurface creates a complex phase profile to generate the gradient and helical wavefront at the same time, so that pure optical vortices can be created at the designed diffraction direction. Our design will find a large amount of applications in compact OAM-multiplexers for free-space and fiber optical communication, OAM based micro- and nanoscale photonic integrated circuits, and other new metasurface devices for complex phase manipulation.

## AUTHOR INFORMATION

### Corresponding Authors

*E-mail: (X.Y.) yangxia@mst.edu.
*E-mail: (J.G.) gaojie@mst.edu.

### Author Contributions

The manuscript was written through contributions of all authors. All authors have given approval to the final version of the manuscript.

### Notes

The authors declare no competing financial interest.

## ACKNOWLEDGMENTS

The authors acknowledge support from the Office of Naval Research under Grant N00014-16-1-2408 and the National Science Foundation under Grant DMR-1552871. The authors also acknowledge the facility support from the Materials Research Center at Missouri S&T.

## REFERENCES

(1) Wang, J.; Willner, A. *Optical Fiber Communication Conference* **2014**, W4J−5.
(2) Allen, L.; Beijersbergen, M. W.; Spreeuw, R.; Woerdman, J. *Phys. Rev. A: At., Mol., Opt. Phys.* **1992**, *45*, 8185.
(3) Kohel, J. M.; Ramirez-Serrano, J.; Thompson, R. J.; Maleki, L.; Bliss, J. L.; Libbrecht, K. G. *J. Opt. Soc. Am. B* **2003**, *20*, 1161−1168.
(4) Wang, J.; Yang, J.-Y.; Fazal, I. M.; Ahmed, N.; Yan, Y.; Huang, H.; Ren, Y.; Yue, Y.; Dolinar, S.; Tur, M. *Nat. Photonics* **2012**, *6*, 488−496.
(5) Richardson, D.; Fini, J.; Nelson, L. *Nat. Photonics* **2013**, *7*, 354−362.
(6) Zhao, Z.; Wang, J.; Li, S.; Willner, A. E. *Opt. Lett.* **2013**, *38*, 932−934.
(7) Zeng, J.; Wang, X.; Sun, J.; Pandey, A.; Cartwright, A. N.; Litchinitser, N. M. *Sci. Rep.* **2013**, *3*, 2826.
(8) Yu, N.; Genevet, P.; Kats, M. A.; Aieta, F.; Tetienne, J.-P.; Capasso, F.; Gaburro, Z. *Science* **2011**, *334*, 333−337.
(9) Yang, Y.; Wang, W.; Moitra, P.; Kravchenko, I. I.; Briggs, D. P.; Valentine, J. *Nano Lett.* **2014**, *14*, 1394−1399.
(10) Wang, W.; Li, Y.; Guo, Z.; Li, R.; Zhang, J.; Zhang, A.; Qu, S. *J. Opt.* **2015**, *17*, 045102.
(11) Sun, J.; Zeng, J.; Litchinitser, N. M. *Opt. Express* **2013**, *21*, 14975−14981.
(12) Sun, J.; Wang, X.; Xu, T.; Kudyshev, Z. A.; Cartwright, A. N.; Litchinitser, N. M. *Nano Lett.* **2014**, *14*, 2726−2729.
(13) Niv, A.; Biener, G.; Kleiner, V.; Hasman, E. *Opt. Express* **2006**, *14*, 4208−4220.
(14) Meinzer, N.; Barnes, W. L.; Hooper, I. R. *Nat. Photonics* **2014**, *8*, 889−898.
(15) Litchinitser, N. M. *Science* **2012**, *337*, 1054−1055.
(16) Li, G.; Kang, M.; Chen, S.; Zhang, S.; Pun, E. Y.-B.; Cheah, K.; Li, J. *Nano Lett.* **2013**, *13*, 4148−4151.
(17) Karimi, E.; Schulz, S. A.; De Leon, I.; Qassim, H.; Upham, J.; Boyd, R. W. *Light: Sci. Appl.* **2014**, *3*, e167.
(18) Hasman, E.; Kleiner, V.; Biener, G.; Niv, A. *Appl. Phys. Lett.* **2003**, *82*, 328−330.
(19) Bomzon, Z. e.; Kleiner, V.; Hasman, E. *Opt. Lett.* **2001**, *26*, 1424−1426.
(20) Bomzon, Z. e.; Biener, G.; Kleiner, V.; Hasman, E. *Opt. Lett.* **2002**, *27*, 285−287.
(21) Arbabi, A.; Horie, Y.; Bagheri, M.; Faraon, A. *Nat. Nanotechnol.* **2015**, *10*, 937−943.
(22) Arbabi, A.; Horie, Y.; Bagheri, M.; Faraon, A. 2014, arXiv preprint; 1411.1494. http://arxiv.org/abs/1411.1494.
(23) Zeng, J.; Gao, J.; Luk, T. S.; Litchinitser, N. M.; Yang, X. *Nano Lett.* **2015**, *15*, 5363−5368.
(24) Genevet, P.; Yu, N.; Aieta, F.; Lin, J.; Kats, M. A.; Blanchard, R.; Scully, M. O.; Gaburro, Z.; Capasso, F. *Appl. Phys. Lett.* **2012**, *100*, 013101.
(25) Hakobyan, D.; Magallanes, H.; Seniutinas, G.; Juodkazis, S.; Brasselet, E. *Adv. Opt. Mater.* **2016**, *4*, 306−312.
(26) Yao, J.; Liu, Z.; Liu, Y.; Wang, Y.; Sun, C.; Bartal, G.; Stacy, A. M.; Zhang, X. *Science* **2008**, *321*, 930−930.



DOI: 10.1021/acs.nanolett.6b00360
*Nano Lett.* 2016, 16, 3101−3108

(27) Yang, X.; Yao, J.; Rho, J.; Yin, X.; Zhang, X. *Nat. Photonics* **2012**, *6*, 450−454.
(28) Alù, A.; Engheta, N. *Phys. Rev. E* **2005**, *72*, 016623.
(29) Sun, L.; Gao, J.; Yang, X. *Phys. Rev. B: Condens. Matter Mater. Phys.* **2013**, *87*, 165134.
(30) Li, S.; Wang, J. *IEEE Photonics J.* **2013**, *5*, 7101007.
(31) Kotlyar, V. V.; Elfstrom, H.; Turunen, J.; Almazov, A. A.; Khonina, S. N.; Soifer, V. A. *J. Opt. Soc. Am. A* **2005**, *22*, 849−861.
(32) Oemrawsingh, S. S. R.; Van Houwelingen, J. A. W.; Eliel, E. R.; Woerdman, J. P.; Verstegen, E. J. K.; Kloosterboer, J. G.; t Hooft, G. W. *Appl. Opt.* **2004**, *43*, 688−694.
(33) Berry, M. V. *Proc. R. Soc. London, Ser. A* **1984**, *392*, 45−57.
(34) Berry, M. V. *J. Mod. Opt.* **1987**, *34*, 1401−1407.
(35) Bhandari, R. *Phys. Lett. A* **1995**, *204*, 188−192.
(36) Gori, F. *Opt. Lett.* **1999**, *24*, 584−586.
(37) Lin, D.; Fan, P.; Hasman, E.; Brongersma, M. L. *Science* **2014**, *345*, 298−302.
(38) Wolf, O.; Campione, S.; Benz, A.; Ravikumar, P. A.; Liu, S.; Luk, T. S.; Kadlec, A. E.; Shaner, A. E.; Klem, F. J.; Sinclair, B. M.; Brener, I. *Nat. Commun.* **2015**, *6*, 7667.
(39) Liu, L.; Zhang, X.; Kenney, M.; Su, X.; Xu, N.; Ouyang, C.; Shi, Y.; Han, J.; Zhang, W.; Zhang, S. *Adv. Mater.* **2014**, *26*, 5031−5036.
(40) Chen, X.; Huang, L.; Mühlenbernd, H.; Li, G.; Bai, B.; Tan, Q.; Jin, G.; Qiu, C.-W.; Zhang, S.; Zentgraf, T. *Nat. Commun.* **2012**, *3*, 1198.
(41) Huang, L.; Chen, X.; Bai, B.; Tan, Q.; Jin, G.; Zentgraf, T.; Zhang, S. *Light: Sci. Appl.* **2013**, *2*, e70.
(42) Zhang, X.; Tian, Z.; Yue, W.; Gu, J.; Zhang, S.; Han, J.; Zhang, W. *Adv. Mater.* **2013**, *25*, 4567−4572.
(43) Ding, F.; Wang, Z.; He, S.; Shalaev, V. M.; Kildishev, A. V. *ACS Nano* **2015**, *9*, 4111−4119.
(44) Kildishev, A. V.; Boltasseva, A.; Shalaev, V. M. *Science* **2013**, *339*, 1232009.
(45) Huang, Y.; Zhao, Q.; Kalyoncu, S. K.; Torun, R.; Lu, Y.; Capolino, F.; Boyraz, O. *Appl. Phys. Lett.* **2014**, *104*, 161106.
(46) Bazhenov, V.; Vasnesov, M. V.; Soskin, M. S. *JETP. Lett.* **1990**, *52*, 429−431.
(47) Gibson, G.; Courtial, J.; Padgett, M.; Vasnetsov, M.; Pasko, V.; Barntt, S.; Frank-Annold, S. *Opt. Express* **2004**, *12*, 5448−5456.
(48) Lin, J.; Genevet, P.; Kats, M. A.; Antoniou, N.; Capasso, F. *Nano Lett.* **2013**, *13*, 4269−4274.
(49) Ge, S.; Ji, W.; Cui, G.; Wei, B.; Hu, W.; Lu, Y. *Opt. Mater. Express* **2014**, *4*, 2535−2541.
(50) Bauer, T.; Banzer, P.; Karimi, E.; Orlov, S.; Rubano, A.; Marrucci, L.; Santamato, E.; Boyd, R. W.; Leuchs, G. *Science* **2015**, *347*, 964−966.



DOI: 10.1021/acs.nanolett.6b00360
*Nano Lett.* 2016, 16, 3101−3108